Proceedings of the Thirty-fifth (2025) International Ocean and Polar Engineering Conference **www.isope.org**
Seoul/Goyang, Korea, June 1-6, 2025

ISBN 978-1-880653-74-6; ISSN 1098-6189

Regular Wave Run-up and Air Entrainment around a Circular Cylinder Based on Adaptive Cartesian Grids

*Mengdi Shi, Jiaying Liu, Weiwen Zhao, Decheng Wan**

Computational Marine Hydrodynamics Lab (CMHL), School of Naval Architecture, Ocean and Civil Engineering,
Shanghai Jiao Tong University, Shanghai, China

*Corresponding Author

ABSTRACT

In this paper, numerical simulation and flow field characteristic analysis of the regular wave run-up around a fixed circular cylinder is achieved by employing self-developed modules for wave generation and wave-structure interaction based on the adaptive mesh refinement framework *Basilisk*. To validate the accuracy of wave generation, the numerical waves are compared with the theoretical results. Meanwhile, different scales of grids are used to verify the grid convergence. The response amplitude operators (RAOs) of surface elevations obtained are compared with experimental results and numerical results computed using the self-developed solver *naoe-FOAM-SJTU*. Various wave parameters are selected to analyze the influence of wave steepness on the flow field characteristics around the cylinder. The evolution process of the free surface, the secondary crest phenomenon and wave scattering are discussed. Air entrainment is innovatively explicated. The study indicates that the *Basilisk* solver can efficiently and accurately capture the complex flow field characteristics of regular wave run-up on a circular cylinder with high computility utilization.

KEY WORDS: wave run-up; multiphase flow; air entrainment; Basilisk

INTRODUCTION

With the exploitation of marine resources turning into the deep ocean, floating platforms become widely used and play a significant role in offshore projects. Most floating platforms are structured with columns such as SPAR and TLP. But under extreme sea conditions, the waves will climb up along the columns and may even reach the bottom deck, which is also known as wave run-up. Severe wave run-up causes huge thumping pressure and splashing, thus threatening the stability and life span of the platform. To avoid potential economic and life losses, it is necessary to study wave run-up on columns of pillar-type platforms and make reasonable designs to decrease its influence.

Numerous scholars have carried out many studies on wave run-up through physical experiments, theoretical analysis, and CFD methods. Galvin and Hallermeier (1972) discovered that the steep wave run-up is mainly affected by the wave scattering and viscous dissipation at the wake region of the cylinder. Swan and Sheikh (2015) conducted the model experiment on a surface-piercing column and specified two types of high-frequency wave scattering, explaining the scattering effects in detail. Wang et al. (2022) improved the accuracy of the wave run-up measurement method based on image recognition. They completed the frame extraction method of the collected videos according to the given sampling frequency and established the time series image set. Through image calibration, grayscale, threshold calculation, and wave surface recognition to obtain the wave surface data, the measurement results of wave run-up are obtained.

Theories about wave run-up have also developed fast, including linear and higher-order diffraction theories and semi-empirical correlations. Goda (2010) systematically introduced the random wave theory and its application in the design of offshore structures, generally summarized the wave run-up, and proposed a variety of calculation methods for wave run-up based on empirical formulas that are suitable for different wave conditions and bank slope shapes. Cao et al. (2017) proposed an efficient semi-empirical formula for wave run-up on a circular cylinder considering the scattering parameter ka , and Li et al. (2022) improved the formula based on the velocity stagnation head theory, which gives a relatively precise prediction for wave run-up.

In recent decades, CFD methods have been widely utilized to study wave run-up. Morgan et al. (2011) used *OpenFOAM* solver to research the interactions between non-linear waves and the cylinder and focused on the influence of computational parameters like grid size, discrete format, and time steps. Sun et al. (2016) made a more detailed study of the nonlinear interactions using a frequency domain potential flow solver *DIFFRACT* and *OpenFOAM* and examined the degree of nonlinearity and the contribution of each harmonic to the free surface run-up and wave forces. Liu (2018) simulated the wave run-up and wave load characterization on a fixed vertical cylinder and discussed the evolution process of free surface and the secondary wave crest phenomenon, based on the independently developed CFD solver *naoe-FOAM-SJTU* for ship and ocean engineering.

However, as the wave run-up generates phenomena such as wave scattering, traditional CFD meshes take splendid computing resources to accurately catch the flow field characteristics around the cylinder and the free surface. The wave crest is prone to numerical dissipation, resulting in the reduction of the simulation accuracy of wave run-up. The adaptive cartesian grids are used in the study in response to this issue. A coarse Cartesian mesh is uniformly generated over the entire region initially. As the simulation processes, grids will be subdivided in quadtree or octree mode until the mesh density at the curve boundaries meets the requirements at computationally demanding areas. This method is characterized by high efficiency and accuracy and is ideal for fine simulation of wave run-up.

The numerical simulation is based on the open-source solver *Basilisk* (Popinet, 2009), with the embedded boundary method utilized to simulate curved solid boundaries and the Volume of Fluid method adopted to track the free surface. The velocity-inlet boundary wave-generating method and momentum source absorption method are used to generate and absorb the first-order Stokes waves. The study implements the simulation of wave run-up on the cylinder with high computility utilization and analyzes the typical physical phenomena such as secondary crest and wave scattering. In addition, air entrainment and characteristics of different stages of wave run-up are innovatively proposed.

METHODOLOGY

Governing equations

The open-source solver *Basilisk* is adopted to solve the two-phase incompressible viscous Navier-Stokes equation. The governing equations in the present solver are as follows:

$$\frac{\partial \rho}{\partial t} + \nabla \cdot (\rho \boldsymbol{U}) = 0 \tag{1}$$

$$\rho\left[\frac{\partial \boldsymbol{U}}{\partial t} + \boldsymbol{U}(\nabla \cdot \boldsymbol{U})\right] = -\nabla p + \mu \nabla^2 \boldsymbol{U} + \rho \boldsymbol{g} + \boldsymbol{f_\sigma} + \boldsymbol{S} \tag{2}$$

where, ρ is the fluid density, $\boldsymbol{U}$ is the fluid velocity, t is the time, p is the fluid pressure, μ is the fluid dynamic viscosity, $\boldsymbol{g}$ is the gravitational acceleration, $\boldsymbol{f_\sigma}$ is the surface tension term functioning only on the surface, and $\boldsymbol{S}$ is the momentum source term which functions only in the damping zone.

Interface capturing

The Volume of Fluid method is used to capture the free surface, and the transport equation can be described below:

$$\frac{\partial \alpha}{\partial t} + \nabla(\boldsymbol{U}\alpha) = 0 \tag{3}$$

where, α indicates the relative proportion of fluid in each cell and its value ranges from 0 to 1. As the study deals only with the two-phase flow, α meets the requirements:

$$\begin{cases} \alpha = 0 & air \\ 0 < \alpha < 1 & interface \\ \alpha = 1 & water \end{cases} \tag{4}$$

The embedded boundary method is used to deal with the curved cylinder boundaries. By considering the volume factions of the intersections between the mesh and the embedded boundary, the method allows the sharp representation of a solid body inside a cartesian mesh and avoids generating complex grids. The detailed calculation process is given in the work by Schwartz (2006).

Wave generation

The study adopts the velocity-inlet boundary wave-generating method to create regular waves by defining the fluid speed and wave height on the inlet boundary. The self-developed wave generation module sets the surface elevation at the inlet boundary by defining the fluid volume fraction. The inlet boundary conditions of free surface elevation and wave velocity for first-order Stokes wave are defined as:

$$\eta(x,t) = \frac{H}{2}\cos(kx - \omega t) \tag{5}$$

$$\begin{cases} U_x(x,z,t) = \dfrac{\pi H}{T}\dfrac{\cosh k(z+d)}{\sinh kd}\cos(kx - \omega t) \\ U_z(x,z,t) = \dfrac{\pi H}{T}\dfrac{\sinh k(z+d)}{\sinh kd}\sin(kz - \omega t) \end{cases} \tag{6}$$

where, η is wave surface elevation, H is wave height, k is wave number, L is the wavelength, d is water depth, T is wave period, ω is circle frequency of waves, and t is time. In particular, it is assumed that the velocity perpendicular to the propagation direction (U_y) can be ignored.

Wave absorption

The study uses the momentum source absorption method to decrease the influence of the wave reflection. The momentum attenuation source term added in the governing equation is described below:

$$S_i = -C \cdot \mu \frac{x - x_0}{x_e - x_0} v_i \quad x_0 < x < x_e \tag{7}$$

where, i represents the coordinate direction, S_i is the momentum source term in the i-direction, C is the linear constant depending on the simulation environment coefficient, x_0 and x_e are respectively the x-coordinate values at the front and the end of the damping zone.

Particularly, making the viscous attenuation source term increase with the x-coordinate can avoid the sudden reflection as the wave propagates to the damping zone while making sure the wave is completely dissipated.

NUMERICAL SETUP

Computational model

The study focused on the regular wave run-up on a fixed circular cylinder. The test case is based on the model tests on a truncated surface piercing column performed at MOERI (Ocean Engineering Committee, 2014) and refers to the work of Liu (2018). With the origin set at the center of the fixed cylinder, the CFD computational domain can be described as $-2\lambda < x < 3\lambda \quad -\lambda < y < \lambda \quad -\lambda < z < 0.5\lambda$, where λ is the wavelength.

At the right end, the damping zone with a length of λ is set to avoid wave reflection. Ten wave probes are installed in a radial pattern around the cylinder at two different distances from its surface and divided into pairs depending on different angles to the wave direction. The gap between the circles is about one radius of the cylinder. The numerical tank setup is shown in Fig. 1, where the water depth $d=\lambda$, the cylinder diameter $D=16$ m, and the cylinder draught $H_C=24$ m. The left boundary is set as the velocity-inlet boundary, the right boundary as the pressure-outlet boundary, and the upper and lower boundaries as the no-slip boundaries. The layout of wave probes is given in Fig. 2 and Table 1. The test conditions are listed in Table 2.

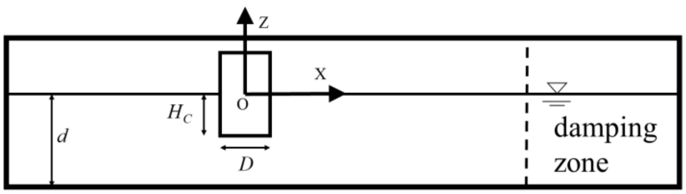

Fig. 1 Side view of the Numerical tank

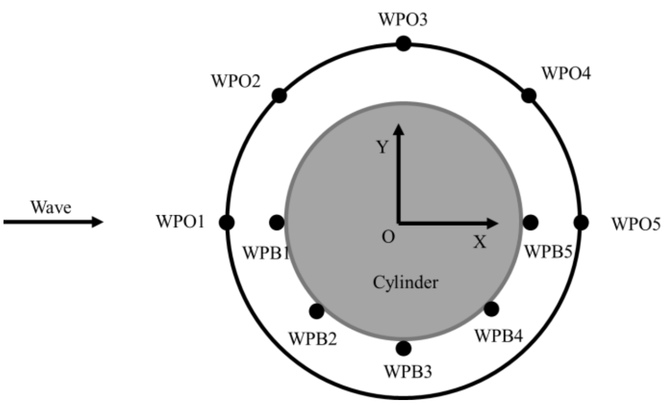

Fig. 2 Layout of the wave probes

Table 1. Coordinates of the wave probes

Inner Circle	x (m)	y (m)	Outer Circle	x (m)	y (m)
WPB1	-8.206	0	WPO1	-16	0
WPB2	-5.803	-5.803	WPO2	-11.314	-11.314
WPB3	0	-8.206	WPO3	0	16
WPB4	5.803	-5.803	WPO4	11.314	11.314
WPB5	8.206	0	WPO5	16	0

Table 2. Test case settings

T	H	λ	H/λ	D/λ
7s	2.548 m	76.44 m	1/30	0.21
	4.777 m		1/16	
	7.644 m		1/10	

The simulation is based on the adaptive mesh refinement framework *Basilisk*. At the initial moment, the mesh is uniformly generated over the entire region and particularly refined around the cylinder. During the simulation, the mesh is adaptively refined according to the volume fraction field and velocity field as Fig. 3 shows. The maximum refinement level is $l_{\max}$, equivalent to the total cells $2^{3l_{\max}}$ in the three-dimension simulation.

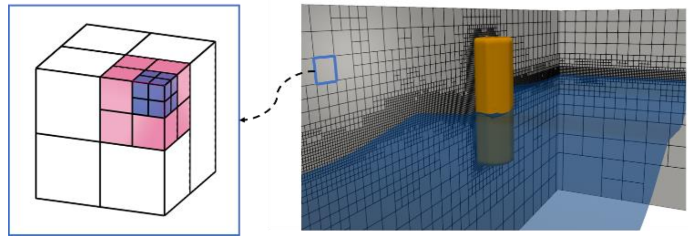

Fig. 3 Refined grids at $t=37.6$ s ($H/\lambda=1/16$)

The grids close to the cylinder and the free surface are intense, especially in the area where waves interact with the cylinder. And the farther away from the surface of the cylinder and the interface, the coarser the mesh is. Therefore, the total number of cells is efficiently decreased, which is useful to increase computing efficiency and accuracy with the same or even less amount of grids.

Convergence analysis

To validate the accuracy of the numerical methods, a mesh convergence study based on the wave-generating experiment is carried out. Three sets of grids with different maximum refinement levels are used for waves at $H=2.548$ m. The surface elevations at the left boundary and comparison with theoretical results are presented in Fig. 4 and Table 3, where ζ is the surface elevation.

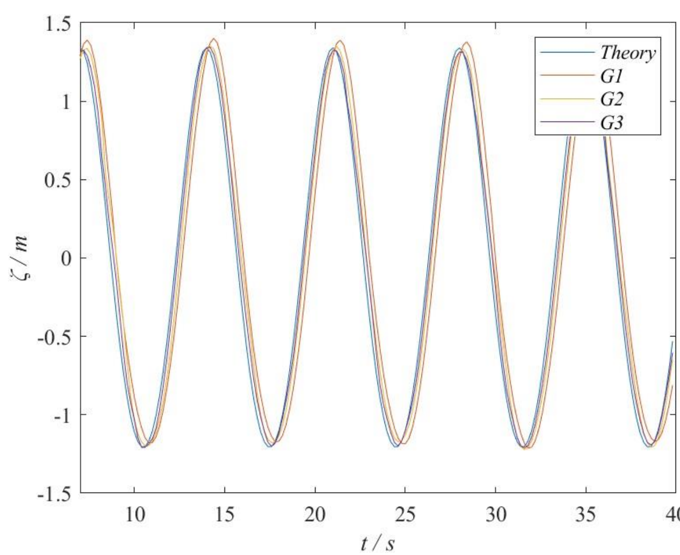

Fig. 4 Time histories of the surface elevations at the left boundary

Table 3. Comparison of surface elevations at the left boundary

Number	$l_{\max}$	Total Cells	Mean Squared Error of H
G1	8	3.11×10^5	7.94%
G2	9	1.22×10^6	4.04%
G3	10	4.59×10^6	0.96%

From the results, the stable waveforms of different groups are almost identical and match the theory well, which indicates that the numerical methods effectively reflect the physical phenomenon studied. Considering the results have already converged in G1 and stay within tolerance in G2 and G3, the maximum refinement level is set to 9 in the subsequent study, as a balance of the calculating efficiency and result accuracy.

RESULTS AND DISCUSSIONS

Wave run-up validation

To verify the correctness of the wave run-up simulation and prepare for further research on the wave characterization, the study compares the computed response amplitude operator (RAO) results with experimental results and simulation results of self-developed solver *naoe-FOAM-SJTU* (Liu, 2018) for free surface elevations. The RAO of surface elevations is defined as the ratio of the wave amplitude at the wave probes to incident wave amplitude and reflects the characterization of wave response under the influence of the linear wave. RAOs for first harmonics at the inner circle of wave probes (WPB1, WPB4, WPB5) and outer circle of wave probes (WPO1, WPO4, WPO5) are shown in Fig. 5.

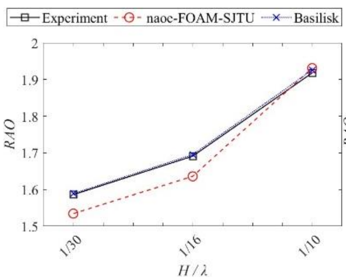

(a)WPB1

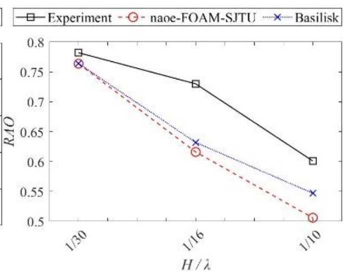

(b)WPB4

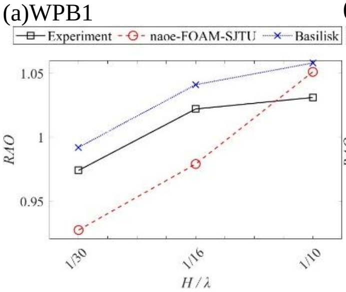

(c)WPB5

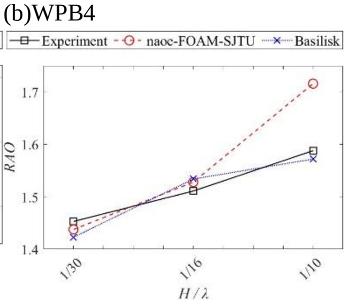

(d)WPO1

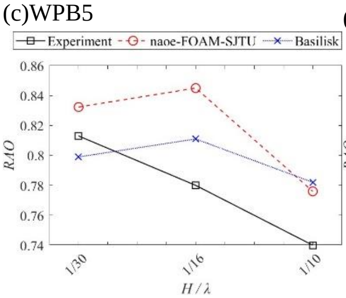

(e)WPO4

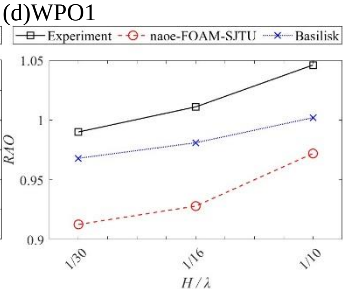

(f)WPO5

Fig. 5 Comparison of RAOs (first harmonics) of surface elevations

From the figures, the numerical results agree well with experimental results and have smaller errors than the results of *naoe-FOAM-SJTU* in general. The correctness of the wave run-up simulation is verified. At the wave probes WPB1 and WPO1 in front of the cylinder, the RAOs are particularly close to experimental results and increase with steepness. It indicates the fact that as the wave steepens, the wave run-up strengthens in front of the cylinder. At the wave probes WPB4 and WPO4 in the shoulders of the cylinder, the RAOs share a similar varying trend with the experimental results but the errors get bigger. As RAOs here decrease with the wave steepness, they reflect the nonlinearity of the nearby flow field. At the wave probes WPB5 and WPO5 in the back of the cylinder, the numerical results are relatively smaller than the experimental results though they have a similar increasing trend. Based on the results, the wave run-up strengthens both in the front and back of the cylinder but weakens in the shoulders. This variation is reduced at the outer circle of wave probes.

Note that at the inner circle of wave probes where the waves have direct complicated interactions with the cylinder, the results are precise in particular, which shows the high internal fineness of numerical methods. The average number of total cells in the simulation is about 1.4 million, which is relatively less than the cells of 1.7 million in the work of Liu. Considering the results of smaller errors, the accuracy and efficiency of adaptive mesh refinement are verified.

Wave run-up analysis

According to the RAO analysis, the flow field exhibits widely different properties in different regions around the cylinder, roughly demarcated by the shoulders of the cylinder. The wave at $H/\lambda = 1/16$ is chosen for further analysis.

Fig. 6~7 show the time histories of surface elevations and frequency spectra at typical wave probes WPB1 and WPB4, where f is the frequency.

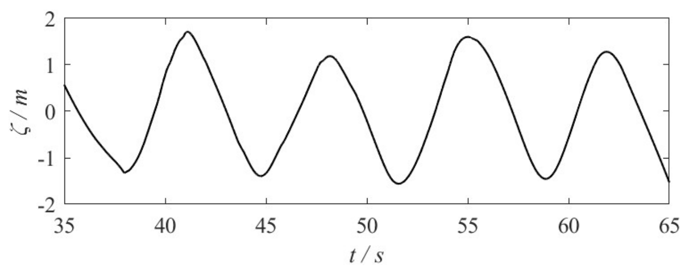

(a) Time histories of surface elevations

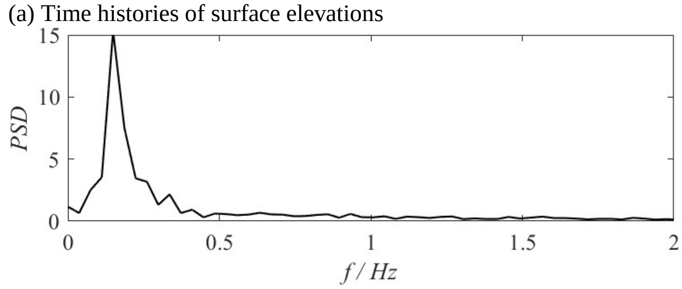

(b)Frequency spectra of surface elevations

Fig. 6 Time histories and frequency spectra at WPB1

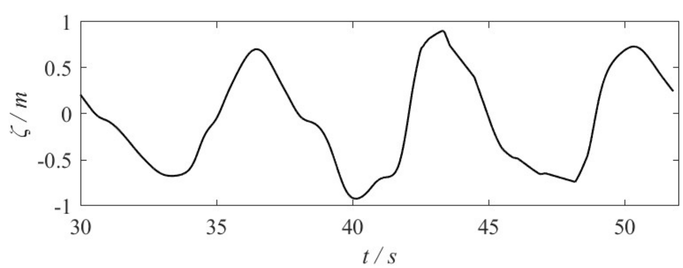

(a) Time histories of surface elevations

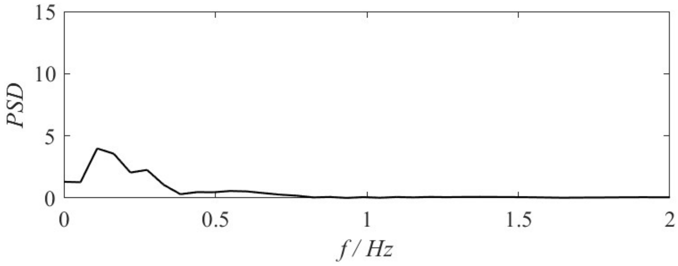

(b)Frequency spectra of surface elevations

Fig. 7 Time histories and frequency spectra at WPB4

In front of the cylinder, the wave keeps a steady and regular shape and the frequency is concentrated at 0.14 Hz, which is also close to the frequency of the incident wave. The flow field presents good regularity and linearity and corresponds to the increasing RAO with wave steepness well. Behind the shoulders of the cylinder, the secondary crest phenomenon is observed and the wave height is the smaller, reflecting the strong irregularity and nonlinearity. This is due to the superposition of the incident wave and reversed circulating flow. When the wave approaches the cylinder, the disturbance drives the elevations in front of the cylinder to flow in two directions around the cylinder and meet at the back. Then part of the currents continue to flow upstream and get superimposed with the incident wave. From the frequency spectrum, the second-order amplitude of the surface elevations at 0.3 Hz is slightly smaller than the first-order amplitude and even a faint third-order amplitude occurs at 0.6 Hz.

Based on the analysis above, the wave run-up process is concluded. When the wave reaches the front surface of the cylinder, the block of the cylinder drives the water to run up and down along its surface at the same frequency as the incident wave. The amplitude is larger than the incident wave and increases linearly with wave steepness. The circulating currents are also developed and begin to flow around the cylinder. As the wave propagates on the sides of the cylinder to the back of the cylinder, the evenly bisected incident waves meet the reversed circulating flow and cause strong nonlinear interactions like the secondary crest phenomenon. The superimposed wave features the decomposed wave frequency and lower amplitude. After the bisected waves merge at the back of the cylinder, the water run-up similar to the one in front of the cylinder with smaller surface elevations occurs. And the merged wave progressively regains its original characteristics.

It is necessary to note that there is a certain amount of noise in the surface elevation data, which is caused by the self-written wave probing function, as there are few related developments on *Basilisk*. The noise results in the deformation of waveforms and affects the second-order amplitude to some extent. The physical offset at the wave crest leads into a non-zero mean value of surface elevation, which is the main reason for the magnitude at 0^{th} frequency. Though it has little effect on qualitative findings, improving the wave probing function is an important part of future improvements.

Wave scattering analysis

For further analysis of the flow phenomenon, the scattered wave fields at $H/\lambda = 1/16$ are plotted in Fig. 8 . The wave scattering process during a period can be divided into 4 phases, which matches the physical experiment results specified by Swan and Sheikh (2015).

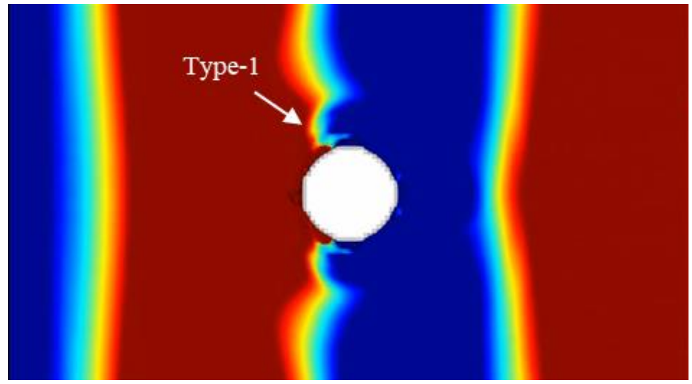

(a)Type-1 waves generating

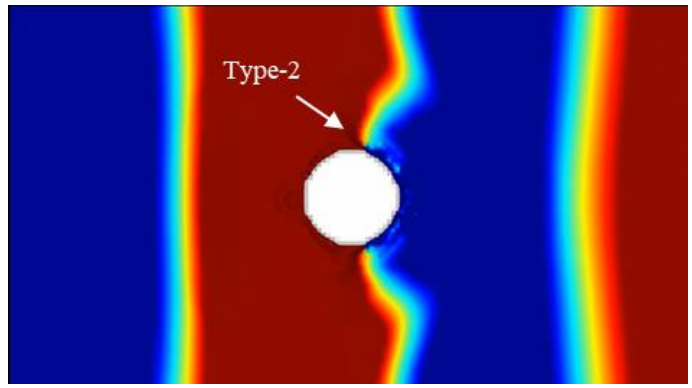

(b)Type-2 waves generating

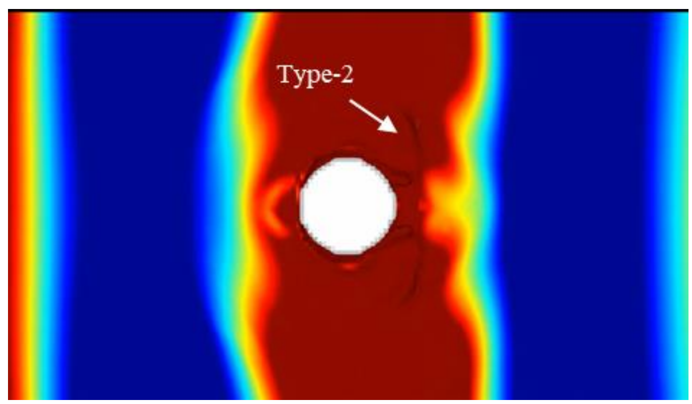

(c)Type-2 waves moving downstream

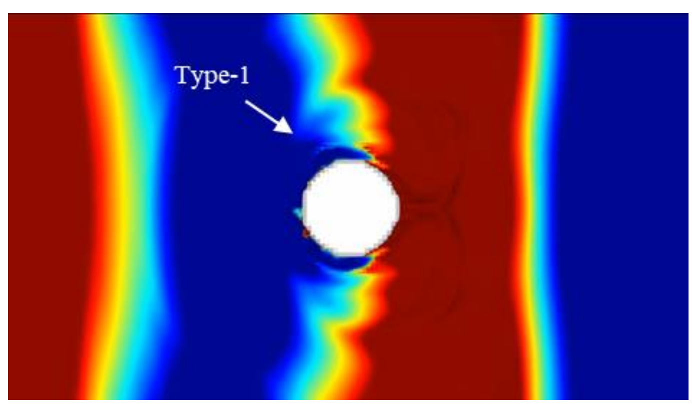

(d)Type-1 waves of wave trough generating

Fig. 8 Scattered wave fields around the cylinder

As the wave crest approaches the cylinder, water is forced to run up and wash down on the front surface of the cylinder due to part of the disturbance, which generates a scattered wave field concentric to the cylinder (Type-1) in (a). When the wave crest reaches the cylinder, the other part of the disturbance drives the elevation flow around both sides of the cylinder and meets at the back surface of the cylinder. Then the circulations continue to propagate around the cylinder and flow back upstream to interact with incident waves, which develops another kind of scattered wave field non-concentric to the cylinder (Type-2) in the shoulders of the cylinder as (b) shown. The Type-2 wave is larger than Type-1 as it involves the superposition of two waves. After the wave crest passes the column, the Type-2 scattered wave fields also move downstream of the cylinder as (c) shown. (b) and (c) demonstrate that Type-2 waves scatter both at the sides of the cylinder and in the downstream direction. Finally, the wave trough approaches the cylinder and Type-1 scattered wave fields appear again in (d) with a smaller amplitude, which is the only scattered wave fields generated by the wave trough. Two Type-1 waves are developed respectively by the wave crest and the wave trough in each cycle. Compared with the experimental results, the wave scattering shares the same generating pattern and properties despite slightly faster dissipation. The influence of the reflecting waves is much less due to the absence of sidewall and the damping zone in the downstream direction. It is concluded that the simulation catches the two types of scattered wave fields accurately.

The Type-1 wave concentric to the cylinder features linearity and affects the surface elevations in the upstream direction mainly. Strong nonlinearity is a notable character of Type-2 scattered wave fields, mainly resulting from the superposition of two kinds of waves. The Type-2 fields have a complex higher-order influence on the nearby flow field characteristics while transferring from the shoulders to the down-wave side, which contributes to the strong nonlinear interactions at WPB4 mentioned in Wave Run-up Process Analysis. As the two Type-2 waves are merged in the back of the cylinder, the surface elevations get disturbed and slightly deviate from the incident wave heights.

Air entrainment

During the wave run-up, a certain amount of air is entrained into the water and tiny bubbles are generated. The study is based on the simulation results at $H/\lambda = 1/16$. Fig. 9 shows the time history of the total air volume entrained during the wave run-up, where V is the instantaneous total volume of air. The whole process can be divided into three phases. During the phase Ⅰ $t = 0 \sim 0.25T$, as the wave crest approaches the cylinder, the water continues to climb up and wash down on the front surface and catch air at the same time.

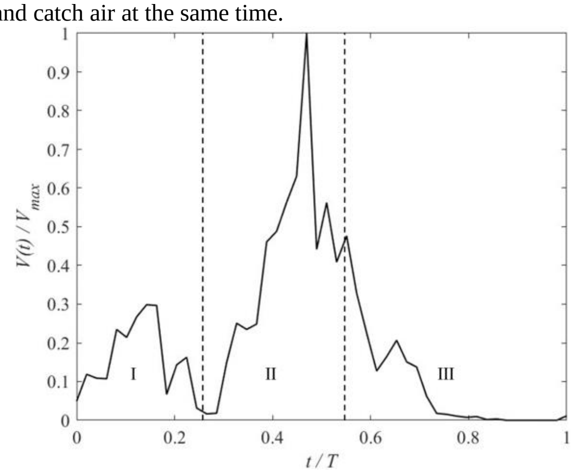

Fig. 9 Time history of total entrained air volume

During the phase, the wave crest thumps the cylinder and then passes through. A large volume of gas is entrained and the total air volume reaches the highest peak. During the phase , existing bubbles get dissipated and almost no new gas is entrained. The total volume slowly decreases to zero.

Fig. 10 shows the bubbles' general spatial distribution, where N is the amount of bubbles. Fig. 11 shows the average results of bubble size distribution in each cycle, where r is the bubble radius. From the figures, bubbles are centrally generated on the front and back surfaces of the cylinder, especially at $0°$ and $180°$ to the wave direction where the wave make strong action on the cylinder. Most bubbles are small with a size less than $r = 0.4$ mm. In phase Ⅰ, the air gets rolled in the water to form even medium-sized cavities at $r = 0.2$ mm. These bubbles clustered directly in front of the cylinder. In phase Π, two processes begin along with the crest hitting the cylinder. First, the strong interaction causes that a large amount of air is entrained and big cavities at $r = 0.3 \sim 0.4$ mm are formed. Second, the medium-sized bubbles from the previous phase break into tiny bubbles at $r = 0.1$ mm. The two processes last from $t = 0.25T$ to $t = 0.55T$ in front of the cylinder. Then, a series of bubbles at around $r = 0.2$ mm are generated at the back of the cylinder when the two flows driven by disturbance around the cylinder meet as Wave Scattering Analysis mentioned. In Phase Ш, the wave generally passes the cylinder, and bubbles are dissipated.

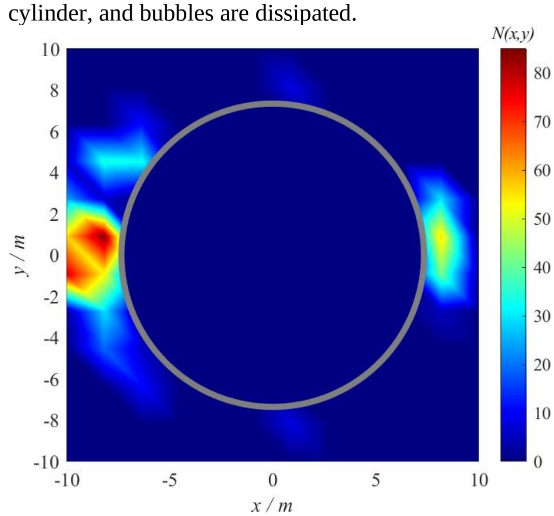

Fig. 10 Number density distribution of bubbles

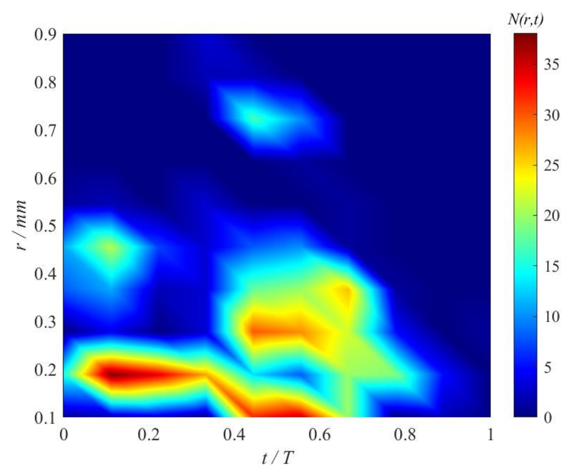

Fig. 11 Average bubble size distribution

CONCLUSIONS

In this paper, numerical simulation and flow field characteristic analysis of the regular wave run-up on a fixed vertical circular cylinder is achieved. The study indicates that the *Basilisk* solver can efficiently and accurately capture the complex flow field characteristics of regular wave run-up around a circular cylinder, and the wave parameters significantly change the flow characteristics during the wave run-up process. The main conclusions are shown below:

(1)A convergence study is carried out for waves at $H = 2.548$ m, whose results agree well with the theory. The convergence of the grids and the effectiveness of the numerical methods are validated.

(2) Compared with the results of the self-developed solver naoe-FOAM-SJTU, the RAOs of surface elevations at different wave steepness give better agreement with the experimental results, which validates the accuracy and efficiency of adaptive mesh refinement.

(3) By analyzing the time histories and frequency spectra of surface elevations in different positions, the flow field presents linearity in front of and behind the cylinder and nonlinearity in the shoulders. The superposition of the incident waves and reversed circulating flow develops the significant secondary crest phenomenon.

(4) The analysis of the flow field around the cylinder indicates that the simulation accurately catches the four phases of wave scattering. Two types of scattered wave fields are identified. The nonlinear Type-2 waves contribute to the nonlinearity in the shoulders of the cylinder.

(5) The study of air entrainment divides the whole process into three phases according to the instantaneous entrained air volume. The causes, sizes, and distribution patterns of bubbles at each stage are innovatively explicated.

ACKNOWLEDGEMENT

This work is supported by the National Natural Science Foundation of China (52131102), to which the authors are most grateful.

REFERENCES

Cao, D., Huang, Z., He, F., Jian, W., & Lo, E. Y.-M. (2017). "An Improved Prediction for Wave Runup on a Circular Cylinder," *Coastal Engineering Journal*, 59(3), 1750013-1 – 1750013-19.

Galvin, C. J., and Hallermeier, R. J. (1972). "Wave run-up on vertical cylinders," *Proc. 13th Int. Conf. Coastal Eng.*, Vancouver, Canada,, 1955-1974

Goda, Y. (2010). *Random Seas and Design of Maritime Structures (3rd Edition)*. Singapore: World Scientific Publishing Co Pte Ltd.

Li, J., Ji, X., Yue, L., & Liu, S. (2022). "An improved method for calculating the wave run-up on a vertical cylinder based on the velocity stagnation head theory," *Ocean Engineering*, 266, 112915.

Liu Z., Wan D. (2018). "Numerical simulation of regular wave run-up on a circular cylinder," *Proceedings of the 29th national conference on hydrodynamics*, 2, 1163-1174

Morgan, G. C. J., Zang, J., Greaves, D., Heath, A., Whitlow, C., & Young, J. (2011). "Using the RasInterFoam CFD model for wave transformation and coastal modeling," *Proceedings of Conference on Coastal Engineering*, (32), 23.

Ocean Engineering Committee. (2014) "Final report and recommendations to the 27th ITTC," Denmark, Copenhagen.

Popinet, S. (2009). "An accurate adaptive solver for surface-tension-driven interfacial flows," *Journal of Computational Physics*, 228(16), 5838–5866.

Schwartz, P., Barad, M., Colella, P., & Ligocki, T. (2006). "A Cartesian grid embedded boundary method for the heat equation and Poisson's equation in three dimensions," *Journal of Computational Physics*, 211(2), 531–550.

Sun, L., Zang, J., Chen, L., Eatock Taylor, R., & Taylor, P. H. (2016). "Regular waves onto a truncated circular column: A comparison of experiments and simulations," *Applied Ocean Research*, 59, 650–662.

Swan, C. and Sheikh, R. (2015) "The interaction between steep waves and a surface-piercing column," *Philosophical transactions of the Royal Society of London. Series A: Mathematical, physical, and engineering sciences*, 373, 2033.

Trulsen, K., & Teigen, P. (2002). "Wave scattering around a vertical cylinder: Fully nonlinear potential flow calculations compared with low order perturbation results and experiment," *Proc. 21st Int. Conf. Offshore Mech. And Artic Eng*, Oslo, Norway.

Wang, J., Wang S., and Chen S. (2022) "Measurement method of wave runup based on image recognition," *Journal of Tianjin University of Technology*, 38, 48–52.